

Neural Image Representations for Multi-Image Fusion and Layer Separation

Seonghyeon Nam Marcus A. Brubaker Michael S. Brown
 York University
 {shnnam, mab, mbrown}@eecs.yorku.ca

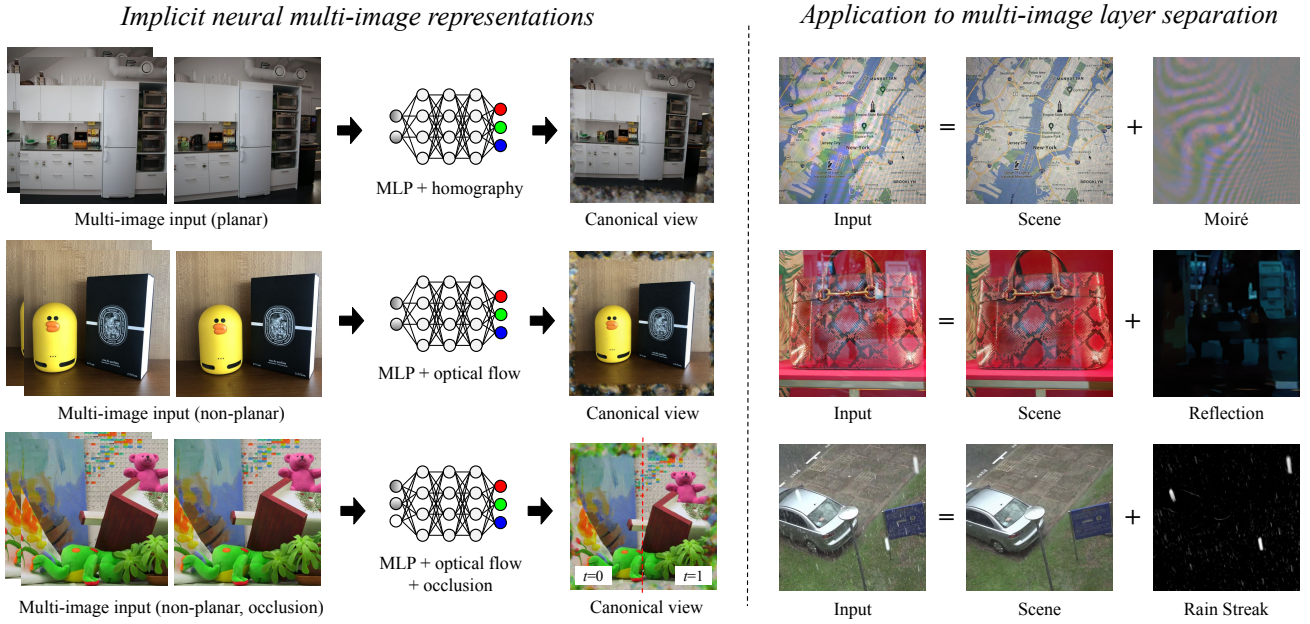


Figure 1: Overview of this paper. In this work, we propose to fuse multiple images into a single canonical view by incorporating image transformation techniques into continuous neural functional representations. Each image is rendered by transforming input coordinates fed into the neural representations using homography or optical flow. We demonstrate the effectiveness of our method on various applications of multi-image layer separation.

Abstract

We propose a framework for aligning and fusing multiple images into a single coordinate-based neural representations. Our framework targets burst images that have misalignment due to camera ego motion and small changes in the scene. We describe different strategies for alignment depending on the assumption of the scene motion, namely, perspective planar (i.e., homography), optical flow with minimal scene change, and optical flow with notable occlusion and disocclusion. Our framework effectively combines the multiple inputs into a single neural implicit function without the need for selecting one of the images as a reference frame. We demonstrate how to use this multi-frame fusion

framework for various layer separation tasks.

1. Introduction and Related Work

Fusing multiple misaligned images into a single view is a fundamental problem in computer vision. The underlying assumption for this task is that the multiple image represent varying view point of the same scene with possible motion in the scene. Many computer vision tasks rely on the multi-image fusion such as image stitching [16, 13, 6], high dynamic range (HDR) imaging [11, 39, 38], image super-resolution [5, 4, 36]. To merge images, it is first essential to align them using techniques such as a homography or optical flow according to the movement of scene. Traditionally,

images are aligned to a reference image that is manually chosen among the input images. Since image pixels are represented in a 2D discrete sampled array, such transformation is approximated by interpolation techniques.

Recently, implicit or coordinate-based neural representations were proposed to represent a single or multiple image(s) as a function of pixel coordinates parameterized by multi-layer perceptrons (MLPs) [33, 30]. This new type of image representations is different from conventional discrete grid-based representations in that image signals are continuous with respect to spatial or spatio-temporal pixel coordinates. Besides, the resolution of images no longer depends on the size of discrete grid, but relies on the complexity of MLPs. The neural representations have been actively studied particularly in view synthesis [25, 31, 28, 15, 23], 3D geometry [24, 26], and image synthesis [32, 2, 29].

In this paper, we are interested in performing multi-frame fusion using continuous functional representations. As shown on the left in Fig. 1, we propose to train MLPs to reconstruct a canonical view where all the information of multiple images are fused, which is achieved by incorporating image registration techniques into the parameterization of neural representations. Unlike existing multi-image fusion, our method does not need an explicit reference image. Instead, a virtual reference image of canonical view is implicitly learned in neural representations. Since the space of canonical view is unbounded, all images can be fused regardless of the original image frame as shown in the figure. In addition, image transformation is achieved in a real-valued coordinate space without interpolation as the function is continuous. To the best of our knowledge, our work is the first to address multi-image fusion in the domain of implicit coordinate-based neural representations.

To demonstrate the effectiveness of the implicit neural multi-image representations, we apply our method to various applications of multi-image layer separation. As shown in Fig. 1, the goal of multi-image layer separation is to decompose signals in multiple images into the underlying scene and interference layer so as to improve the visibility of the underlying scene. Many multi-image approaches for different tasks have been studied such as image demoiré [12, 37], reflection removal [14, 1, 19, 20], fence removal [19, 20], and deraining [10, 40, 7, 35]. Early works on these problems heavily rely on domain-specific priors for optimization, while recent approaches are driven by deep learning and a large amount of annotated data for supervision.

In our work, we cast the problem as an unsupervised optimization of multi-image neural representations. Specifically, we fuse the underlying scene from the multiple images using to a single neural representation. Depending on the type of scene motion, we use different alignment strategies when computing the neural representation. To remove

the interference layer, we propose two-stream neural representations. In particular, the underlying “clean layer” image without interference is represented by one neural implicit function, while a separate neural implicit function is used to represent the interference layer(s). We show that standard regularization terms – for example, total variation – can be used in the optimization of these neural implicit functions to assist in the layer separation. We demonstrate the effectiveness of our approach on moiré removal, obstruction removal, and rain removal.

A closely related work to ours is the Double DIP work [9]. Double DIP also studied image layer decomposition on a single or multiple image(s) using coupled deep image priors [34]. The Double DIP exploits self-similarity, an inductive bias in convolutional neural networks (CNNs), to separate different signals. Our approach uses the parameterization of motion as a general prior to tackle multiple tasks. Unlike semantic segmentation and matting [9, 22], we focus on disentangling low-level signals rather than semantic layers.

2. Method

Neural image representations have recently been proposed [30, 33] which represent RGB values of an image as a function of pixel coordinates parameterized by neural networks. In the case of multiple sequential images, such functions are formulated as

$$\hat{\mathbf{I}}_{(x,y,t)} = f_{\theta_I}(x, y, t), \quad (1)$$

where $\hat{\mathbf{I}}_{(x,y,t)}$ is a pixel value of t -th frame at the spatial position (x, y) and f_{θ_I} is a neural network that has parameters θ_I . In this form, each frame is represented independently at the different value of t .

In our work, we assume our multiple images are captured quickly in a burst manner from a single camera. This means the images are approximately of the same scene, but have small variations among the images due to motion of the camera and motion in the scene. Furthermore, the capture from the same camera within a short time duration means we do not expect variations in scene lighting or colors due to camera color manipulation.

Within this context of burst images, our work aims to formulate f_{θ_I} differently by learning a joint representation of multiple images using their spatio-temporal correlation. To this end, we revisit well-established techniques of image registration and motion compensation in the new domain of coordinate-based neural representations. Specifically, our f_{θ_I} learns a canonical view of the scene shared across images. Each image is rendered by projecting the canonical view on the plane of the image using motion compensation methods such as a perspective planar transform (*i.e.*, a homography) or pixel-wise optical flow. Since the function is

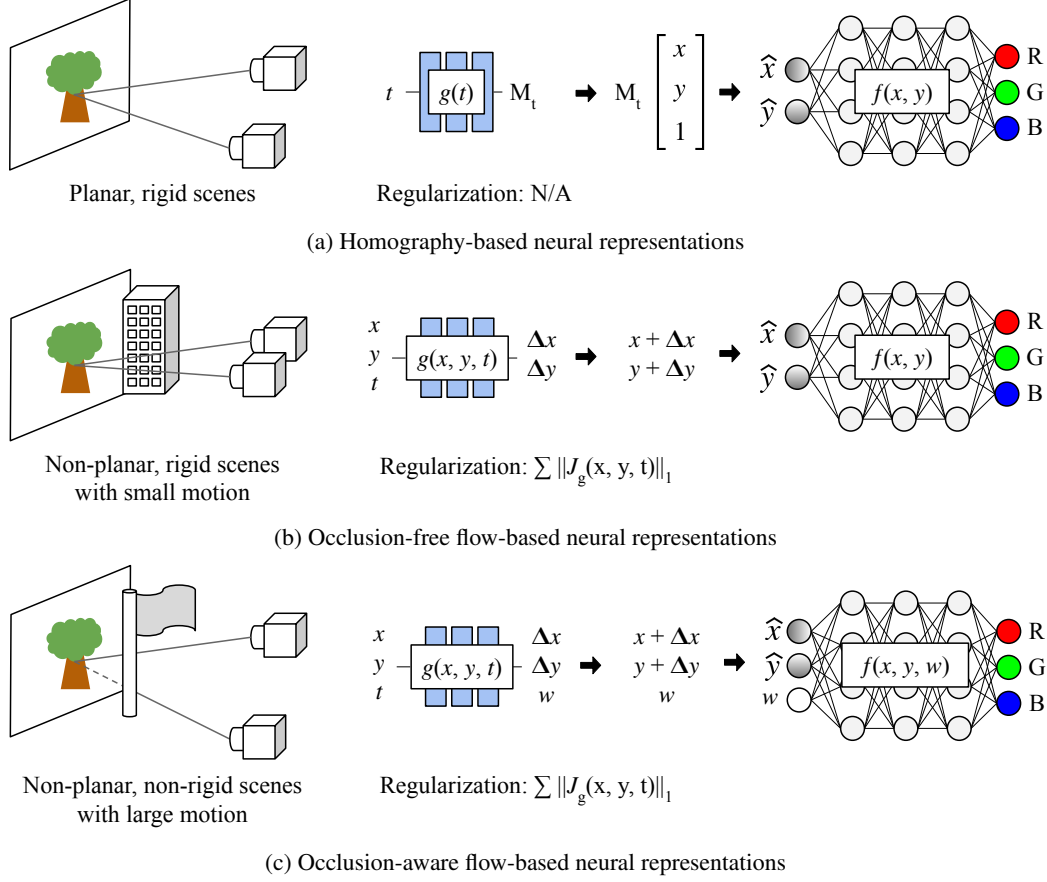


Figure 2: Overview of our explicit motion-based neural representations. (a), (b), and (c) show homography-based neural representations, occlusion-free flow-based neural representations, and occlusion-aware flow-based neural representations, respectively.

continuous and unbounded, it is able to not only store the entire scene regardless of the size of 2D image grid, but also be projected onto each image by transforming input coordinates in a real-valued space. The rendering process is formally described as

$$\hat{\mathbf{I}}_{(x,y,t)} = f_{\theta_I}(T(g_{\theta_T}(x, y, t), (x, y, t))), \quad (2)$$

where g_{θ_T} is a function that estimates the parameters of a coordinate transform, and a generic function T transforms the coordinates of each frame to their corresponding positions on the canonical view. The parameters of two networks θ_T and θ_I are optimized by minimizing the following pixel reconstruction loss:

$$\mathcal{L}_{\text{Recon}} = \sum \|\hat{\mathbf{I}}_{(x,y,t)} - \mathbf{I}_{(x,y,t)}\|_2^2, \quad (3)$$

where \mathbf{I} is a ground truth.

The explicit parameterization of motion in neural representations is advantageous in that it enables the simultaneous learning of image and motion representations. By

minimizing Eq. (3), our neural representations learn the parameters of scene motion in an unsupervised manner. More importantly, unlike conventional image registration and motion compensation techniques, no reference image is required by our approach. Instead, our neural representation learns a virtual reference view of the scene implicitly.

Using our multi-frame alignment framework, we demonstrate various applications of multi-image layer separation. The problem is to decompose the underlying scene and interference in burst or multi-frame images. To address this, we focus on the fact that the movement of the underlying scene and the interference layer is usually different. As the explicit motion-based neural representations have an inductive bias towards motion, two signals can be separated by the difference of motion. To do this, we propose a two-stream architecture of neural representations.

In the following, we describe our formulation of the explicit motion-based neural representations and two-stream neural representations for multi-image layer separation in detail.

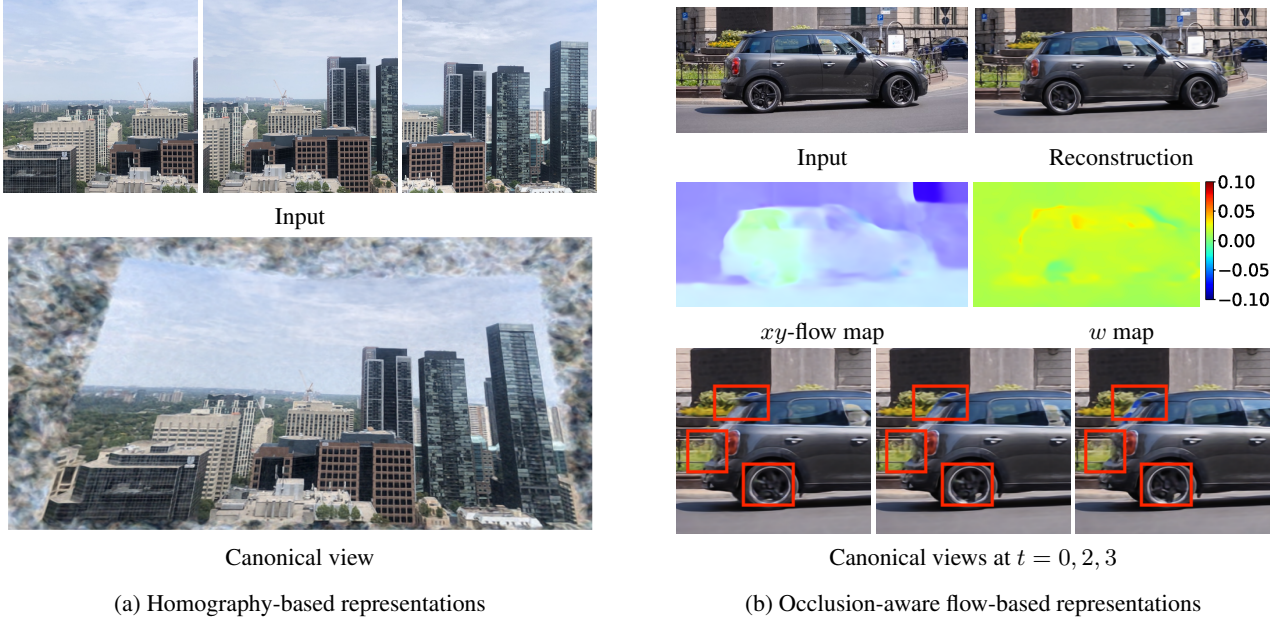


Figure 3: Visualization of learned representations. In (a), the top row shows 3 of 9 representative images used to learn a homography-based neural representation, and the bottom shows a learned canonical view. In (b), the first row shows one of the input and reconstruction images, the second row shows a xy -flow map and w map learned by an occlusion-aware flow-based representation, and the third row shows canonical views at $t = 0, 2, 3$.

2.1. Neural image representations for multi-image fusion

Fig. 2 shows the overview of the neural image representations for multi-image fusion. We propose three kinds of parameterization according to the assumption of the scene: (a) homography-based neural representations, (b) occlusion-free flow-based neural representations, and (c) occlusion-aware flow-based neural representations.

Homography-based neural representations. In case of planar and rigid scenes moving globally as shown in Fig. 2 (a), we use homography as a parameterization of coordinate transformation. As shown in the figure, g_{θ_T} is learned to estimate parameters of a homography matrix M for each frame. The rendering of images using the homography-based neural representations is formally described as:

$$\hat{\mathbf{I}}_{(x,y,t)} = f_{\theta_I}(M_t[x, y, 1]^T), \quad (4)$$

where M_t is a 3×3 linear matrix represented as $M_t = g_{\theta_T}(t)$. Since M_t is applied globally regardless of spatial coordinates, $g_{\theta_T}(t)$ only takes t as input. We omit the normalization of output coordinates for simplicity.

Fig. 3 (a) shows a visualization of learned representation. For training, we capture 9 consecutive images of a scene in a large distance by moving a camera horizontally from left to right. As can be seen in the figure, the homography-based

neural function automatically stitches all the images in a single view only using a reconstruction loss. Each image is rendered by projecting the canonical view onto the image plane using a learned homography matrix.

Occlusion-free flow-based neural representations. In most cases, the movement of scene is not global and parts of a scene move differently since the scene is not planar. As shown in Fig. 2 (b), we use a dense optical flow to model the per-pixel movement of scene, which is represented by the displacement of x and y coordinates. We assume that the motion is small enough to cause no or little occlusion and disocclusion. Here, g_{θ_T} estimates a dense xy -flow for given (x, y, t) , which is formulated as $(\Delta x_t, \Delta y_t) = g_{\theta_T}(x, y, t)$, where Δx_t and Δy_t are the displacement of x and y coordinates. The output image is rendered by the following equation:

$$\hat{\mathbf{I}}_{(x,y,t)} = f_{\theta_I}(x + \Delta x_t, y + \Delta y_t). \quad (5)$$

In addition to the reconstruction loss in Eq. (3), we use a total variation (TV) regularization for the smoothness of flow, which is described as

$$\mathcal{L}_{\text{TVFlow}} = \sum \|J_{g_{\theta_T}}(x, y, t)\|_1, \quad (6)$$

where $J_{g_{\theta_T}}(x, y, t)$ is a Jacobian matrix that consists of gradients of g_{θ_T} with respect to x, y , and t .

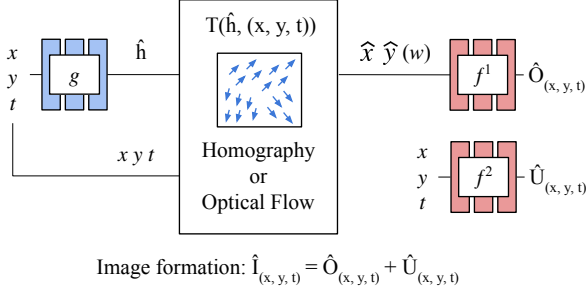


Figure 4: Overview of our two-stream neural representations for multi-image layer separation.

Occlusion-aware flow-based neural representations.

Since the canonical view of the occlusion-free flow-based neural representations is in a 2D plane, it is not enough to store extra information when a scene is occluded or disoccluded. To address such cases, we add an additional dimension w of canonical view as shown in Fig. 2 (c). Intuitively, different versions of a scene at a certain position caused by occlusion are stored at different values of w , while occlusion-irrelevant pixels are stored at the same value of w and shared across images. This is achieved by regularizing the Jacobian of g_{θ_T} in Eq. (6). With w , the output image is rendered by the following equation:

$$\hat{\mathbf{I}}_{(x,y,t)} = f_{\theta_I}(x + \Delta x_t, y + \Delta y_t, w_t). \quad (7)$$

Fig. 3 (b) shows a visualization of a learned xy -flow map, w map, and canonical views at different values of w after training five consecutive images in [27]. Since the car is moving in the scene, the xy -flow map shows spatially varying optical flow on the car. Particularly, the w map shows different values in occluded parts. As can be seen in red boxes in canonical views, different values of w store occluded contents. For non-occluded parts, the image in the leftmost column is used.

2.2. Two-stream neural representations for multi-image layer separation

We apply the implicit multi-image neural representations to multi-image layer separation. To this end, we use two neural functions $f_{\theta_O}^1$ and $f_{\theta_U}^2$ to learn the underlying scene and interference, respectively. Fig. 4 shows the overview of our two-stream neural representations, and two functions are formulated as

$$\begin{cases} \hat{\mathbf{O}}_{(x,y,t)} &= f_{\theta_O}^1(T(g_{\theta_T}(x, y, t), (x, y, t))), \\ \hat{\mathbf{U}}_{(x,y,t)} &= f_{\theta_U}^2(x, y, t). \end{cases} \quad (8)$$

Since we usually have the knowledge of scene motion, we use an explicit parameterization of motion for $f_{\theta_O}^1$. On the other hand, we use an unconstrained form of neural representations for $f_{\theta_U}^2$ to store contents that violate the motion

in $f_{\theta_O}^1$, which is beneficial for interference patterns whose motion is difficult to model. The generic form of image formation is described as

$$\hat{\mathbf{I}}_{(x,y,t)} = \hat{\mathbf{O}}_{(x,y,t)} + \hat{\mathbf{U}}_{(x,y,t)}, \quad (9)$$

but the formation varies according to different tasks. As the degree of freedom of $f_{\theta_U}^2$ is higher than that of $f_{\theta_O}^1$, $f_{\theta_U}^2$ tends to learn the entire contents of images by ignoring $f_{\theta_O}^1$. To prevent it, we suppress $f_{\theta_U}^2$ using a regularization loss formulated as

$$\mathcal{L}_{\text{Interf}} = \sum \|\hat{\mathbf{U}}_{(x,y,t)}\|_1. \quad (10)$$

3. Applications

In this section, we show the effectiveness of our method on various applications of multi-image layer separation with experiments.

3.1. Moiré removal

Moiré pattern is a common pattern of unexpected interference when taking a photo of digital screen using digital cameras. It is caused by the overlapping of pixel grid in display and color filter array in camera sensor, and the pattern differs according to the alignment of two grids. Burst images usually capture temporally varying moiré patterns as camera shake changes the alignment. The movement of the scene in burst images follows homography transform since the screen is planar, while the moiré pattern changes differently. In this subsection, we show that our two-stream neural representations are able to separate the underlying scene and moiré pattern by exploiting the difference of motion.

Formulation. We parameterize $f_{\theta_O}^1$ as a homography-based neural representation in Eq. (4). The image formation follows the basic form in Eq. (9), where we use signed values in the range of $[-1, 1]$ for the output of both $\hat{\mathbf{O}}_{(x,y,t)} \in \mathbb{R}^3$ and $\hat{\mathbf{U}}_{(x,y,t)} \in \mathbb{R}^3$. The signed output for $\hat{\mathbf{U}}_{(x,y,t)}$ is particularly useful to represent color bands of moiré patterns. For optimization, we adopt an exclusion loss used in [9, 41] to enforce the structure of two signals not to correlate with each other, which is formulated as

$$\mathcal{L}_{\text{Excl}} = \sum \|\Phi(J_{f_1}(x, y), J_{f_2}(x, y))\|_2^2, \quad (11)$$

where $\Phi(J_{f_1}(x, y), J_{f_2}(x, y)) = \tanh(N_1 J_{f_1}(x, y)) \otimes \tanh(N_2 J_{f_2}(x, y))$, and \otimes is an element-wise multiplication. N_1 and N_2 are the normalization terms used in [41]. Finally, we optimize θ_T , θ_O , and θ_U using the following training objective:

$$\mathcal{L}_{\text{Moire}} = \mathcal{L}_{\text{Recon}} + \lambda_{\text{Interf}} \mathcal{L}_{\text{Interf}} + \lambda_{\text{Excl}} \mathcal{L}_{\text{Excl}}, \quad (12)$$

where λ_{Interf} and λ_{Excl} are hyperparameters. We implement our method using a multi-layer perceptron with ReLU activation for g_{θ_T} and a SIREN [30] for $f_{\theta_O}^1$ and $f_{\theta_U}^2$.

	AFN [37]	C3Net [12]	D. DIP [9]	Ours
Input	Single	Burst	Burst	Burst
Method	S	S	U	U
PSNR	43.63	27.99	18.53	38.68
SSIM	0.9952	0.8071	0.8762	0.9751
NCC	0.9963	0.7724	0.5120	0.9865
SI	0.9962	0.7721	0.4895	0.9856

Table 1: Quantitative evaluation of moiré removal on a synthetic dataset. AFN [37] uses a single image and other methods use 5 images as input. In Method, S and U indicate a supervised and unsupervised approach, respectively.

Experiments. Since there is no publicly available dataset for multi-frame screen-captured moiré images, we synthesize a dataset from clean images. To do this, we use Slideshare-1M [3] dataset that consists of approximately one million images of university lecture slides to mimic content likely to be captured by students. Using this dataset, we synthesize 100 sequences of 5 burst images for testing following the synthesis procedure in [17].

For comparison, we use three baseline methods: AFN [37], C3Net [12], and Double DIP [9]. AFN and C3Net are state-of-the-art deep learning methods for a single and burst image demoiréing task, respectively. To train them, we synthesize a training set that contains 10,000 sequences. We additionally evaluate Double DIP to compare unsupervised approaches.

Table 1 shows a quantitative comparison of methods on the synthetic test set. In addition to PSNR and SSIM, we compare a Normalized Cross-Correlation (NCC) and Structure Index (SI). Even though our method does not outperform AFN, the performance is significantly better than C3Net and Double DIP, which is reasonable since our method is not trained on a large dataset in a supervised manner. Fig. 5 shows a qualitative evaluation on real images. We capture real images by taking five burst photos of a MacBook display using an iPhone 8 camera. As can be seen, our method outperforms all the baselines on real images. The performance of AFN and C3Net is degraded because they are not trained on real images. Double DIP fails to decompose the underlying scene and moiré pattern since it relies on an inductive bias in convolutional neural networks, which is not enough to separate complex signals. On the other hand, our method removes a moiré pattern by restricting the movement of scene to homography, which acts as a strong prior of moiré removal.

3.2. Obstruction removal

The goal of obstruction removal is to eliminate foreground objects or scenes that hinder the visibility of the

background scene. Obstructions can be in the form of reflection on a window in front of the scene or a physical object such as a fence. We apply the two-stream neural representations based on occlusion-free optical flow to a reflection and fence removal. In this case, the background scenes are not planar, but the movement of the scene is small enough to ignore occlusion. Similarly to moiré removal, we decompose the reflection and fence layer using the fact that they move differently to the background scene.

Formulation. We use the occlusion-free flow-based representations in Eq. (5) for $f_{\theta_O}^1$. For a reflection removal, we use the image formation in Eq. (9) where $\hat{\mathbf{O}}_{(x,y,t)} \in \mathbb{R}^3$ and $\hat{\mathbf{U}}_{(x,y,t)} \in \mathbb{R}^3$ are in the range of $[0, 1]$. We use the following combination of loss functions as a training objective:

$$\begin{aligned} \mathcal{L}_{\text{Refl}} = & \mathcal{L}_{\text{Recon}} + \lambda_{\text{TVFlow}} \mathcal{L}_{\text{TVFlow}} \\ & + \lambda_{\text{Interf}} \mathcal{L}_{\text{Interf}} + \lambda_{\text{Excl}} \mathcal{L}_{\text{Excl}}, \end{aligned} \quad (13)$$

where λ_{TVFlow} is a hyperparameter. For a fence removal, we use a different image formation described as

$$\hat{\mathbf{I}}_{(x,y,t)} = (1 - \alpha_{(x,y,t)}) \hat{\mathbf{O}}_{(x,y,t)} + \alpha_{(x,y,t)} \hat{\mathbf{U}}_{(x,y,t)} \quad (14)$$

where $\hat{\mathbf{O}}_{(x,y,t)} \in \mathbb{R}^3$ and $\hat{\mathbf{U}}_{(x,y,t)} \in \mathbb{R}^3$ are in the range of $[0, 1]$, and $(\alpha_{(x,y,t)}, \hat{\mathbf{U}}_{(x,y,t)}) = f_{\theta_U}^2(x, y, t)$. $\alpha_{(x,y,t)} \in \mathbb{R}$ is a alpha map of the fence layer in the range of $[0, 1]$. The training objective is described as:

$$\mathcal{L}_{\text{Fence}} = \mathcal{L}_{\text{Recon}} + \lambda_{\text{TVFlow}} \mathcal{L}_{\text{TVFlow}} + \lambda_{\text{Interf}} \mathcal{L}_{\text{Interf}}. \quad (15)$$

We use the SIREN neural implicit architecture to implement all the functions.

Experiments. Fig. 6 shows qualitative results of our method and existing approaches. We use real images in [14] for testing. The methods of Li and Brown [14] and Alayrac *et al.* [1] are designed for reflection removal, and the method in [20] is a general approach for obstruction removal. As can be seen, our method is able to accurately decomposes the background scene and reflection compared with the baseline methods. Fig. 7 shows a qualitative comparison of fence removal on real images in [20]. Our method achieves comparable quality of results to learning-based methods that heavily rely on the large amount of data and supervision.

3.3. Rain removal

To show the effectiveness of the occlusion-aware flow-based neural representations, we address the problem of multi-image rain removal as the task deals with various kinds of scenes from static scenes to dynamic scenes. Since rain streaks move fast and randomly, the streaks impact

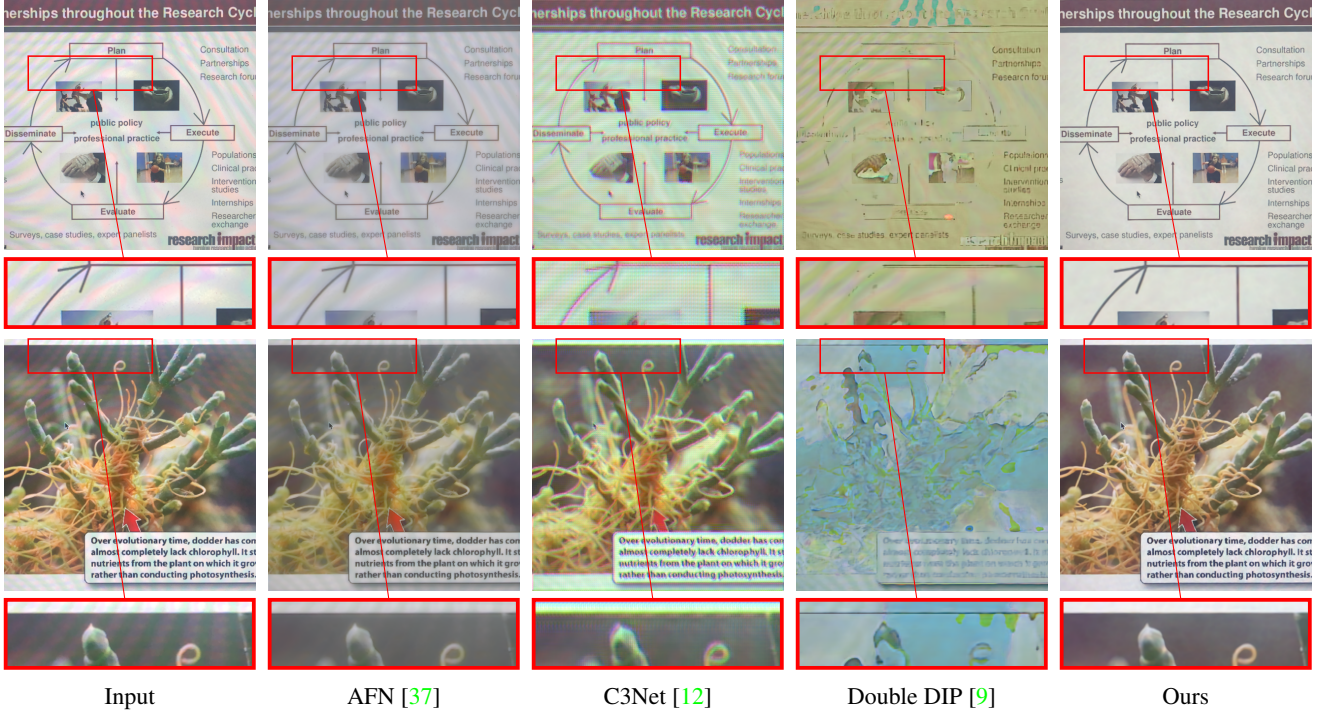


Figure 5: Qualitative comparison of moiré removal on real images.

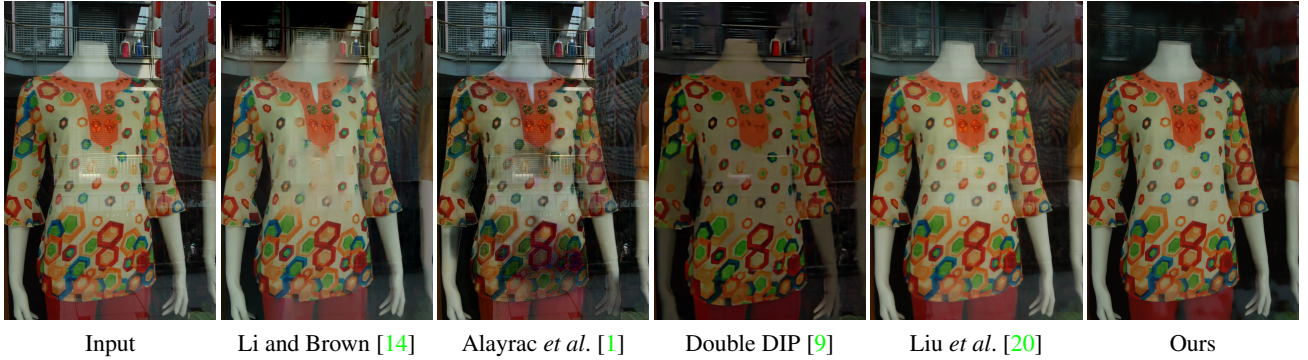


Figure 6: Qualitative results of reflection removal on real images in [14].

the smoothness of the scene motion. We exploit this prior knowledge of the rain streaks randomness in the multiple images by imposing a smoothness regularization of flow map. The underlying assumption is that the scene flow should be smooth and variation in this smooth flow are attributed to the rain streaks we wish to remove.

Formulation. We use the occlusion-aware flow-based neural representations in Eq. (7) as a formulation of $f_{\theta_O}^1$. Since rain streaks are achromatic, we use the following image formation:

$$\hat{\mathbf{I}}_{(x,y,t)} = (1 - \hat{\mathbf{U}}_{(x,y,t)})\hat{\mathbf{O}}_{(x,y,t)} + \hat{\mathbf{U}}_{(x,y,t)}\mathbf{1}, \quad (16)$$

where $\hat{\mathbf{O}}_{(x,y,t)} \in \mathbb{R}^3$ and $\hat{\mathbf{U}}_{(x,y,t)} \in \mathbb{R}$ are in the range of $[0, 1]$, and $\mathbf{1} = [1, 1, 1]^T$. In this form, $\hat{\mathbf{U}}_{(x,y,t)}$ acts as an alpha map of rain streaks. Our final training objective is described as

$$\mathcal{L}_{\text{Rain}} = \mathcal{L}_{\text{Recon}} + \lambda_{\text{TVFlow}}\mathcal{L}_{\text{TVFlow}} + \lambda_{\text{Interf}}\mathcal{L}_{\text{Interf}}. \quad (17)$$

Experiments. Fig. 8 shows a qualitative evaluation on real images in NTURain [8], where cars and pedestrians are moving. We compare state-of-the-art video deraining methods based on optimization [10] and deep learning [7]. We take 5 consecutive images to run our method. As can be seen, our method clearly removes rain streaks in the scene,

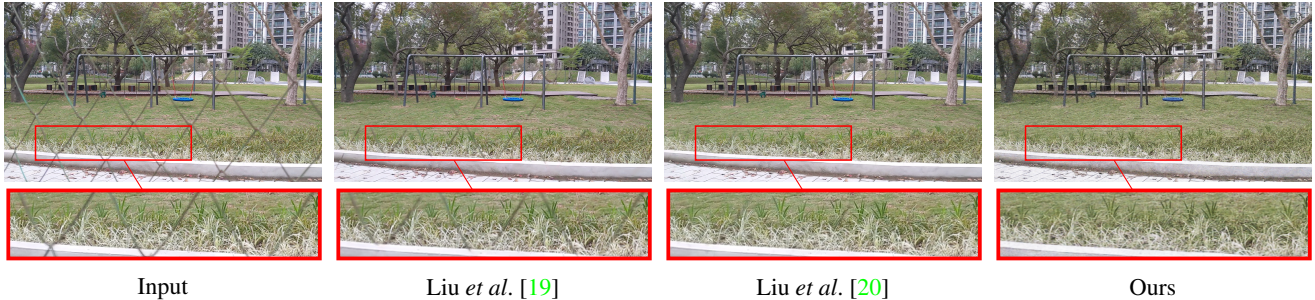


Figure 7: Qualitative comparison of fence removal on real images in [20].

	Supervised		Unsupervised		
	SpacCNN [7]	FCDN [40]	SE [35]	FastDeRain [10]	Ours
PSNR	32.78	35.80	26.56	29.42	28.61
SSIM	0.9239	0.9622	0.8006	0.8683	0.8604

Table 2: Quantitative evaluation of rain removal on RainSynLight25 [18].

which is competitive to the baselines. For quantitative evaluation, we use RainSynLight25 [18] dataset that consists of 25 synthetic sequences of 9 images. Table 2 shows results of ours and state-of-the-art methods: SE [35], FastDeRain [10], SpacCNN [7], and FCDN [40]. Even though our method does not outperform deep learning-based methods, it achieves a comparable result to optimization-based approaches without supervision and the domain knowledge of deraining. We believe that incorporating more priors and regularizations into our method could further improve the performance.

3.4. Discussion

Ablation study on loss functions. We conduct an ablation study on reflection removal to show the effectiveness of various loss functions. In Fig. 9, we show the decomposed background and reflection layer of different training objectives by removing each loss function. As can be seen, the background content is reconstructed in the reflection layer when we do not use $\mathcal{L}_{\text{Interf}}$ since g_{θ_U} is unconstrained. Without $\mathcal{L}_{\text{TVFlow}}$, on the other hand, both signals are reconstructed in the background layer. In this case, g_{θ_O} has enough freedom to learn the mixture of two layers moving differently. In addition to $\mathcal{L}_{\text{Interf}}$ and $\mathcal{L}_{\text{TVFlow}}$, the exclusion loss $\mathcal{L}_{\text{Excl}}$ further improves the quality of decomposition by preventing the structure of two layers from being correlated.

Analysis of w . Fig. 10 shows an ablation study on w in the occlusion-aware flow-based neural representations, which

is the same model as the occlusion-free flow-based neural representations. We use images in the RainSynLight25 dataset for experiment. Therefore, we show the ground truth and PSNR results in the figure. As shown in the red boxes on the output, the method without w produces artifacts around occlusion and disocclusion, which indicates that it is difficult to represent all contents including occlusion in a 2D canonical view. With an additional variable w , our method stores occlusion in the extra dimension, thereby enables the accurate reconstruction shown in the figure.

In Fig. 11, we additionally conduct an experiment to further understand the space represented by w . Specifically, we explicitly enforce our model to represent most of pixel values at $w = 0$ by adding the regularization $\mathcal{L}_w = \sum \|w\|_1$. We also evaluate the performance by training the same model 5 times and computing the mean and standard deviation of PSNRs. As can be seen, the model with \mathcal{L}_w uses 0 as the center of w space, while the original model uses an arbitrary value varying according to initialization. However, the quality of output is similar as shown in both qualitative and quantitative results. This finding implies that the smoothness prior driven by $\mathcal{L}_{\text{TVFlow}}$ is more important to learn multi-image representation than the center of w .

3.5. Other applications

Burst image denoising. We additionally apply our method to burst image denoising. To do this, we cast the problem as a layer separation that is to decompose the signal of images into the underlying scene and noise. In this task, we use an occlusion-free flow-based neural representation as a function of scene, which is reasonable since the motion of burst images is typically small but may not be planar. We use the same objective as used in moiré removal. As shown in Fig. 12, we evaluate the performance using a burst image denoising dataset in [21]. Our method demonstrates a competitive result compared with a burst image denoising method [21], which indicates that the multi-image fusion based on coordinate-based neural representations is also useful to remove random noise signals.

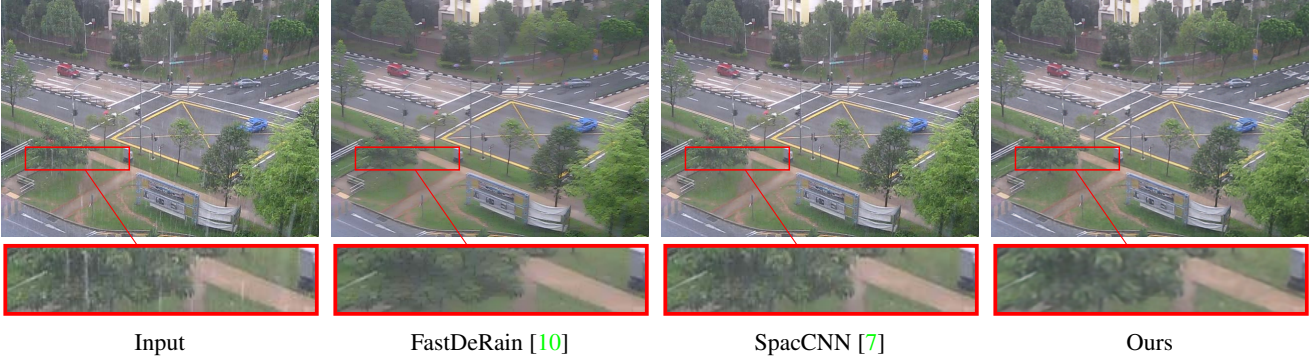


Figure 8: Qualitative comparison of rain removal on real images in NTURain [8].

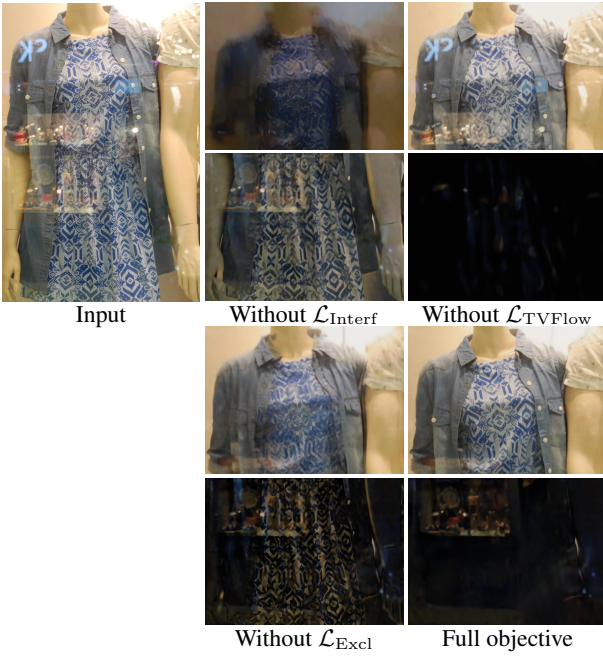


Figure 9: Ablation study of loss functions on reflection removal. The top and bottom image show the background and reflection layer, respectively.

Joint demosaicing and burst super-resolution. To further understand the effectiveness of the multi-image fusion in continuous functional representations, we apply our method to a more challenging task: burst image super-resolution. Since our method deals with a real-valued coordinate space, it is technically applicable to a sub-pixel registration in burst super-resolution. For experiment, we use a real burst dataset in [5, 4] that contains sequences of 14 RAW burst images for testing. To reconstruct RGB values from Bayer color filter array (CFA) images, we multiply a channel mask to the 3-channel output of a neural representation before comparing to ground truth. At inference

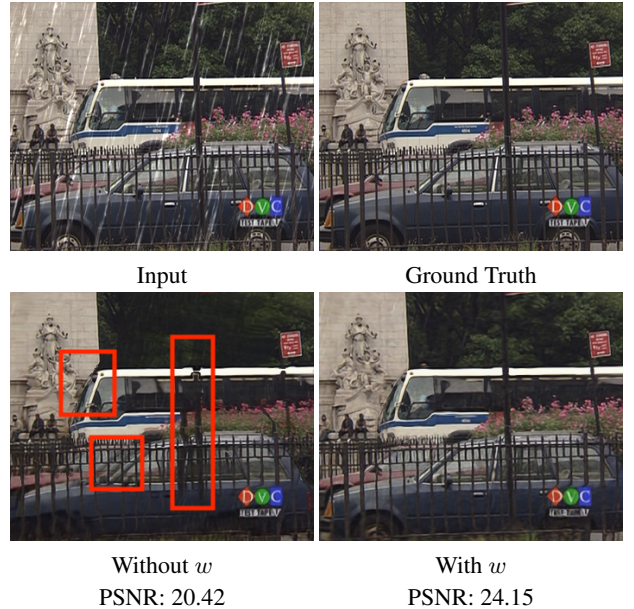


Figure 10: Ablation study on w . Using the synthetic dataset RainSynLight25, we show the ground truth and PSNRs.

time, we take all channels of RGB output, where missing channels are interpolated. For implementation, we use an occlusion-free flow-based neural representation without a two-stream architecture. Fig. 13 shows results of a joint demosaicing and burst super-resolution (x4). The original image is upsampled using a bicubic interpolation, and all images are post-processed using the code in [4]. As can be seen, our results show clearer details of images than bicubic results, but are still blurry. Our conjecture is that the sub-pixel alignment may not be accurate since the optimization only relies on the error of pixel intensities. Thus, an interesting direction of follow-up research would be to add more loss functions and regularization to assist with sub-pixel registration. Image noise is also reduced in our results

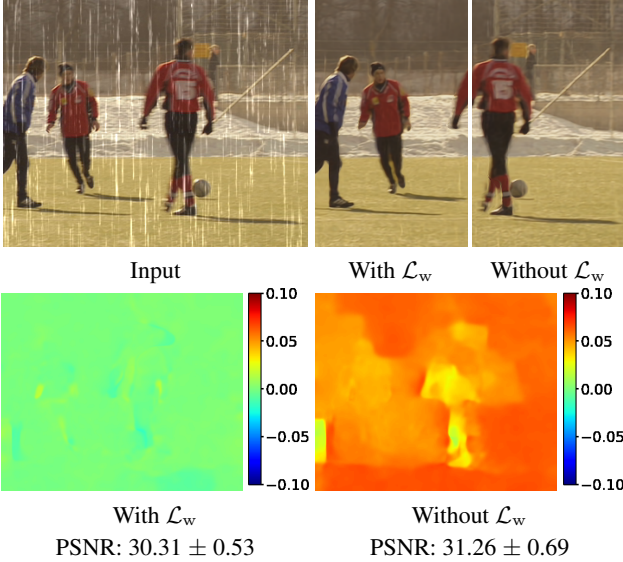


Figure 11: Analysis on w . We apply an additional loss $\mathcal{L}_w = \sum \|w\|_1$ and compare it with the original model. For PSNRs, we train each model 5 times and aggregates results.

without an explicit noise layer, but using two-stream architecture would further improve the performance.

4. Concluding remarks

We have described an optimization framework to fuse multiple input images into a coordinate-based neural representations, in particular the SIREN neural implicit function. Our optimization simultaneously registers the images and fuses them into a single neural representation. We have described variations on this framework for different three underlying scene motion: homography-based, occlusion-free optical flow, and occlusion-aware optical flow. Unlike conventional image alignment and fusion, our approach does not need to select one of the input images as a reference frame. We also showed how to use this multi-frame alignment framework to perform several different types of layer separation problems such as moiré pattern removal, obstruction removal, and noise reduction. For these approaches, we described the use of two neural implicit functions, one for the desired scene layer and the other for the inference layer. Depending on the properties of the interference layer, we described different regularization strategies to achieve the layer separation.

Coordinate-based neural implicit functions are an exciting new representation over traditional 2D-based pixel grid representations. This work represents initial efforts to extend the neural representation to multi-frame inputs for various low-level computer vision tasks.

References

- [1] Jean-Baptiste Alayrac, Joao Carreira, and Andrew Zisserman. The visual centrifuge: Model-free layered video representations. In *IEEE Conf. Comput. Vis. Pattern Recog.*, pages 2457–2466, 2019. 2, 6, 7
- [2] Ivan Anokhin, Kirill Demochkin, Taras Khakhulin, Gleb Sterkin, Victor Lempitsky, and Denis Korzhnikov. Image generators with conditionally-independent pixel synthesis. In *IEEE Conf. Comput. Vis. Pattern Recog.*, pages 14278–14287, 2021. 2
- [3] André Araujo, Jason Chaves, Haricharan Lakshman, Roland Angst, and Bernd Girod. Large-scale query-by-image video retrieval using bloom filters. *arXiv preprint arXiv:1604.07939*, 2016. 6
- [4] Goutam Bhat, Martin Danelljan, and Radu Timofte. Ntire 2021 challenge on burst super-resolution: Methods and results. In *IEEE Conf. Comput. Vis. Pattern Recog. Worksh.*, pages 613–626, 2021. 1, 9
- [5] Goutam Bhat, Martin Danelljan, Luc Van Gool, and Radu Timofte. Deep burst super-resolution. In *IEEE Conf. Comput. Vis. Pattern Recog.*, pages 9209–9218, 2021. 1, 9, 11
- [6] Matthew Brown and David G Lowe. Automatic panoramic image stitching using invariant features. *Int. J. Comput. Vis.*, 74(1):59–73, 2007. 1
- [7] Jie Chen, Cheen-Hau Tan, Junhui Hou, Lap-Pui Chau, and He Li. Robust video content alignment and compensation for rain removal in a cnn framework. In *IEEE Conf. Comput. Vis. Pattern Recog.*, pages 6286–6295, 2018. 2, 7, 8, 9
- [8] Jie Chen, Cheen-Hau Tan, Junhui Hou, Lap-Pui Chau, and He Li. Robust video content alignment and compensation for rain removal in a cnn framework. In *IEEE Conf. Comput. Vis. Pattern Recog.*, pages 6286–6295, 2018. 7, 9
- [9] Yosef Gandelsman, Assaf Shocher, and Michal Irani. ”double-dip”: Unsupervised image decomposition via coupled deep-image-priors. In *IEEE Conf. Comput. Vis. Pattern Recog.*, pages 11026–11035, 2019. 2, 5, 6, 7
- [10] Tai-Xiang Jiang, Ting-Zhu Huang, Xi-Le Zhao, Liang-Jian Deng, and Yao Wang. Fastderain: A novel video rain streak removal method using directional gradient priors. *IEEE Trans. Image Process.*, 28(4):2089–2102, 2018. 2, 7, 8, 9
- [11] Nima Khademi Kalantari, Ravi Ramamoorthi, et al. Deep high dynamic range imaging of dynamic scenes. *ACM Trans. Graph.*, 36(4):144–1, 2017. 1
- [12] Sangmin Kim, Hyungjoon Nam, Jisu Kim, and Jechang Jeong. C3net: Demoiréing network attentive in channel, color and concatenation. In *IEEE Conf. Comput. Vis. Pattern Recog. Worksh.*, pages 426–427, 2020. 2, 6, 7
- [13] Anat Levin, Assaf Zomet, Shmuel Peleg, and Yair Weiss. Seamless image stitching in the gradient domain. In *Eur. Conf. Comput. Vis.*, pages 377–389. Springer, 2004. 1
- [14] Yu Li and Michael S Brown. Exploiting reflection change for automatic reflection removal. In *IEEE Conf. Comput. Vis. Pattern Recog.*, pages 2432–2439, 2013. 2, 6, 7
- [15] Zhengqi Li, Simon Niklaus, Noah Snavely, and Oliver Wang. Neural scene flow fields for space-time view synthesis of dynamic scenes. In *IEEE Conf. Comput. Vis. Pattern Recog.*, pages 6498–6508, 2021. 2



Figure 12: Burst image denoising. We use images in [21].

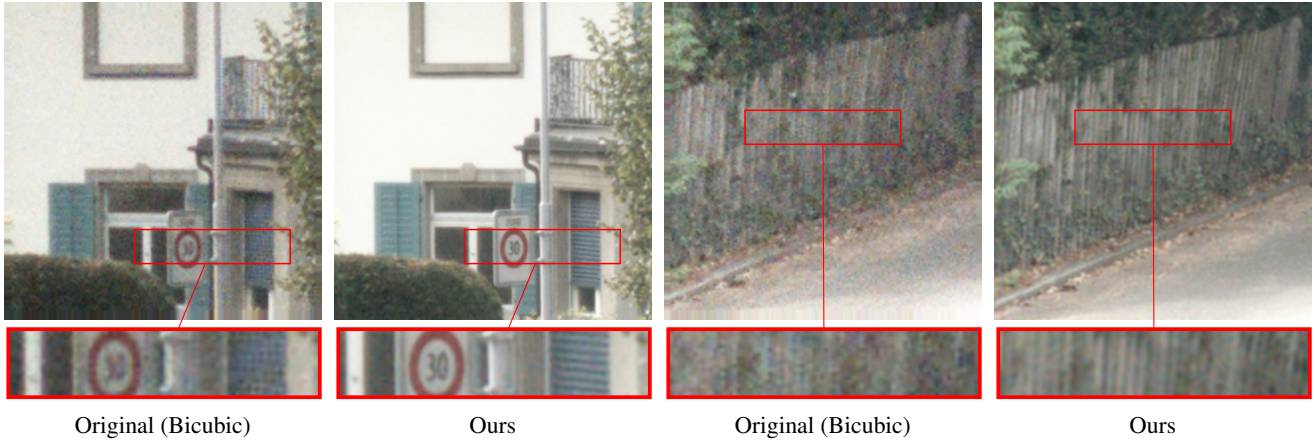


Figure 13: Burst image super-resolution. We use images in [5].

- [16] Chung-Ching Lin, Sharathchandra U Pankanti, Karthikeyan Natesan Ramamurthy, and Aleksandr Y Aravkin. Adaptive as-natural-as-possible image stitching. In *IEEE Conf. Comput. Vis. Pattern Recog.*, pages 1155–1163, 2015. 1
- [17] Bolin Liu, Xiao Shu, and Xiaolin Wu. Demoir\’eing of camera-captured screen images using deep convolutional neural network. *arXiv preprint arXiv:1804.03809*, 2018. 6
- [18] Jiaying Liu, Wenhan Yang, Shuai Yang, and Zongming Guo. Erase or fill? deep joint recurrent rain removal and reconstruction in videos. In *IEEE Conf. Comput. Vis. Pattern Recog.*, pages 3233–3242, 2018. 8
- [19] Yu-Lun Liu, Wei-Sheng Lai, Ming-Hsuan Yang, Yung-Yu Chuang, and Jia-Bin Huang. Learning to see through obstructions. In *IEEE Conf. Comput. Vis. Pattern Recog.*, pages 14215–14224, 2020. 2, 8
- [20] Yu-Lun Liu, Wei-Sheng Lai, Ming-Hsuan Yang, Yung-Yu Chuang, and Jia-Bin Huang. Learning to see through obstructions with layered decomposition. *arXiv e-prints*, pages arXiv–2008, 2020. 2, 6, 7, 8
- [21] Ziwei Liu, Lu Yuan, Xiaoou Tang, Matt Uyttendaele, and Jian Sun. Fast burst images denoising. *ACM Trans. Graph.*, 33(6):1–9, 2014. 8, 11
- [22] Erika Lu, Forrester Cole, Tali Dekel, Andrew Zisserman, William T Freeman, and Michael Rubinstein. Omnimatte: Associating objects and their effects in video. In *IEEE Conf. Comput. Vis. Pattern Recog.*, pages 4507–4515, 2021. 2
- [23] Ricardo Martin-Brualla, Noha Radwan, Mehdi SM Sajjadi, Jonathan T Barron, Alexey Dosovitskiy, and Daniel Duckworth. Nerf in the wild: Neural radiance fields for unconstrained photo collections. In *IEEE Conf. Comput. Vis. Pattern Recog.*, pages 7210–7219, 2021. 2
- [24] Lars Mescheder, Michael Oechsle, Michael Niemeyer, Sebastian Nowozin, and Andreas Geiger. Occupancy networks: Learning 3d reconstruction in function space. In *IEEE Conf. Comput. Vis. Pattern Recog.*, pages 4460–4470, 2019. 2
- [25] Ben Mildenhall, Pratul P Srinivasan, Matthew Tancik, Jonathan T Barron, Ravi Ramamoorthi, and Ren Ng. Nerf: Representing scenes as neural radiance fields for view syn-

- thesis. In *Eur. Conf. Comput. Vis.*, pages 405–421. Springer, 2020. [2](#)
- [26] Jeong Joon Park, Peter Florence, Julian Straub, Richard Newcombe, and Steven Lovegrove. DeepSDF: Learning continuous signed distance functions for shape representation. In *IEEE Conf. Comput. Vis. Pattern Recog.*, pages 165–174, 2019. [2](#)
- [27] Federico Perazzi, Jordi Pont-Tuset, Brian McWilliams, Luc Van Gool, Markus Gross, and Alexander Sorkine-Hornung. A benchmark dataset and evaluation methodology for video object segmentation. In *IEEE Conf. Comput. Vis. Pattern Recog.*, pages 724–732, 2016. [5](#)
- [28] Albert Pumarola, Enric Corona, Gerard Pons-Moll, and Francesc Moreno-Noguer. D-nerf: Neural radiance fields for dynamic scenes. In *IEEE Conf. Comput. Vis. Pattern Recog.*, pages 10318–10327, 2021. [2](#)
- [29] Tamar Rott Shaham, Michaël Gharbi, Richard Zhang, Eli Shechtman, and Tomer Michaeli. Spatially-adaptive pixelwise networks for fast image translation. In *IEEE Conf. Comput. Vis. Pattern Recog.*, pages 14882–14891, 2021. [2](#)
- [30] Vincent Sitzmann, Julien Martel, Alexander Bergman, David Lindell, and Gordon Wetzstein. Implicit neural representations with periodic activation functions. *Adv. Neural Inform. Process. Syst.*, 33, 2020. [2](#), [5](#)
- [31] Vincent Sitzmann, Michael Zollhoefer, and Gordon Wetzstein. Scene representation networks: Continuous 3d-structure-aware neural scene representations. *Adv. Neural Inform. Process. Syst.*, 32:1121–1132, 2019. [2](#)
- [32] Ivan Skorokhodov, Savva Ignatyev, and Mohamed Elhoseiny. Adversarial generation of continuous images. In *IEEE Conf. Comput. Vis. Pattern Recog.*, pages 10753–10764, 2021. [2](#)
- [33] Matthew Tancik, Pratul Srinivasan, Ben Mildenhall, Sara Fridovich-Keil, Nithin Raghavan, Utkarsh Singhal, Ravi Ramamoorthi, Jonathan Barron, and Ren Ng. Fourier features let networks learn high frequency functions in low dimensional domains. In *Adv. Neural Inform. Process. Syst.*, volume 33, 2020. [2](#)
- [34] Dmitry Ulyanov, Andrea Vedaldi, and Victor Lempitsky. Deep image prior. In *IEEE Conf. Comput. Vis. Pattern Recog.*, pages 9446–9454, 2018. [2](#)
- [35] Wei Wei, Lixuan Yi, Qi Xie, Qian Zhao, Deyu Meng, and Zongben Xu. Should we encode rain streaks in video as deterministic or stochastic? In *Int. Conf. Comput. Vis.*, pages 2516–2525, 2017. [2](#), [8](#)
- [36] Bartłomiej Wronski, Ignacio Garcia-Dorado, Manfred Ernst, Damien Kelly, Michael Krainin, Chia-Kai Liang, Marc Levoy, and Peyman Milanfar. Handheld multi-frame super-resolution. *ACM Trans. Graph.*, 38(4):1–18, 2019. [1](#)
- [37] Dejia Xu, Yihao Chu, and Qingyan Sun. Moiré pattern removal via attentive fractal network. In *IEEE Conf. Comput. Vis. Pattern Recog. Worksh.*, pages 472–473, 2020. [2](#), [6](#), [7](#)
- [38] Qingsen Yan, Dong Gong, Qinfeng Shi, Anton van den Hengel, Chunhua Shen, Ian Reid, and Yanning Zhang. Attention-guided network for ghost-free high dynamic range imaging. In *IEEE Conf. Comput. Vis. Pattern Recog.*, pages 1751–1760, 2019. [1](#)
- [39] Qingsen Yan, Lei Zhang, Yu Liu, Yu Zhu, Jinqiu Sun, Qinfeng Shi, and Yanning Zhang. Deep hdr imaging via a non-local network. *IEEE Trans. Image Process.*, 29:4308–4322, 2020. [1](#)
- [40] Wenhan Yang, Jiaying Liu, and Jiashi Feng. Frame-consistent recurrent video deraining with dual-level flow. In *IEEE Conf. Comput. Vis. Pattern Recog.*, pages 1661–1670, 2019. [2](#), [8](#)
- [41] Xuaner Zhang, Ren Ng, and Qifeng Chen. Single image reflection separation with perceptual losses. In *IEEE Conf. Comput. Vis. Pattern Recog.*, 2018. [5](#)